Spectroscopic Confirmation of A Massive Protocluster with Two Substructures at $z \simeq 3.1$

MICHAEL J. NICANDRO ROSENTHAL D, AMY J. BARGER D, 1,2,3 LENNOX L. COWIE D, LOGAN H. JONES D, 1,4 STEPHEN J. MCKAY D, AND ANTHONY J. TAYLOR D, AND ANTHONY J. TAYLOR D, 6

Department of Astronomy, University of Wisconsin-Madison, 475 N. Charter Street, Madison, WI 53706, USA
 Department of Physics and Astronomy, University of Hawaii, 2505 Correa Road, Honolulu, HI 96822, USA
 Institute for Astronomy, University of Hawaii, 2680 Woodlawn Drive, Honolulu, HI 96822, USA
 Space Telescope Science Institute, 3700 San Martin Drive, Baltimore, MD 21218, USA
 Department of Physics, University of Wisconsin-Madison, 1150 University Ave., Madison, WI 53706, USA
 Department of Astronomy, The University of Texas at Austin, Austin, TX, USA

(Received 13 Mar 2024; Revised 31 Oct 2024; Accepted 05 Nov 2024)

Submitted to ApJ

ABSTRACT

We present the results of a Keck and NOEMA spectroscopic survey of 507 galaxies, where we confirm the presence of two massive overdensities at z=3.090-3.110 and z=3.133-3.155 in the neighborhood of the GOODS-N, each with over a dozen spectroscopically confirmed members. We find that both of these have galaxy overdensities of NIR-detected galaxies of $\delta_{\rm gal,obs}=6-9$ within corrected volumes of $(6-7)\times10^3$ cMpc³. We estimate the properties of the z=0 descendants of these overdensities using a spherical collapse model and find that both should virialize by $z\simeq0.5-0.8$, with total masses of $M_{\rm tot}\simeq(6-7)\times10^{14}~\rm M_{\odot}$. The same spherical collapse calculations, as well as a clustering-of-clusters statistical analysis, suggest a >80% likelihood that the two overdensities will collapse into a single cluster with $M_{\rm tot}=(1.0-1.5)\times10^{15}~M_{\odot}$ by $z\sim0.1-0.4$. The z=3.14 substructure contains a core of four bright dusty star-forming galaxies with $\Sigma {\rm SFR}=2700\pm700~{\rm M}_{\odot}~{\rm yr}^{-1}$ in a volume of only 280 cMpc³.

Keywords: High-redshift galaxy clusters (2007); Galaxy evolution (594); Redshift surveys (1378)

1. INTRODUCTION

Galaxy clusters are the largest gravitationally bound structures in the Universe and have a pronounced influence on the evolution of galaxies contained within them. For decades, we have known that galaxies within denser environments, like groups and clusters, tend to be redder, more elliptical, and have lower star formation rates (SFRs) than field galaxies at similar redshifts (e.g., Balogh et al. 1998; Muzzin et al. 2009). This transition toward a "red and dead" galaxy population in dense environments has been shown to be the combined result both of secular feedback and environmental quenching.

Corresponding author: Michael J. Nicandro Rosenthal rosenthal@astro.wisc.edu

At $z \gtrsim 1$, however, this SFR-density relation is inverted, with galaxies in denser environments being much more actively star-forming than those in co-eval field environments (Elbaz et al. 2007; Cooper et al. 2008; Brodwin et al. 2013). This is believed to be at least in part due to time evolution: at early times, the most massive haloes accumulated gas faster in their deeper gravitational potential wells. This accumulation of gas allowed for an earlier onset of star formation, leading to increased SFRs at high redshifts. However, these overdense environments also quenched earlier, due to the relatively early onset of stellar, active galactic nuclei (AGNs), and environmental feedback, resulting in the red and dead population in galaxy clusters today. Understanding this population of protoclusters, the progenitors of today's galaxy clusters, is therefore essential to understand the buildup of mass in the Universe overall.

While large numbers of galaxy clusters have been discovered in wide-field, homogenous surveys out to $z \sim 1.5$ (e.g., Bleem et al. 2015; Balogh et al. 2021), far fewer $z \gtrsim 2$ protoclusters have been confirmed, with largely heterogenous selection (e.g., Casey 2016; Alberts & Noble 2022, and references therein). Unlike nearby clusters, which can be identified by high concentrations of red galaxies (e.g., Muzzin et al. 2009), or thermal Xrays (e.g., Cruddace et al. 2002; Stanford et al. 2006), or Sunyaev-Zeldovich effect signatures (e.g., Bleem et al. 2015) of the hot intracluster medium, protoclusters are not yet virialized (Chiang et al. 2013; Muldrew et al. 2015; Overzier 2016) and have bluer, more highly star-forming galaxies than the field. Protoclusters are therefore identified by the detection of large numbers of star-forming galaxies on ~ 10 cMpc scales (e.g., Overzier 2016, and references therein), with the gold standard being large numbers of spectroscopic detections in a window of $\Delta z \approx 0.02 - 0.03$ (e.g., Casey et al. 2015; Cucciati et al. 2018; Polletta et al. 2021). Due to the expense of spectroscopic observations at the highest redshifts, many $z \gtrsim 3$ protoclusters have only a few—or even a single—spectroscopically confirmed galaxy (e.g., Wang et al. 2021), making it impossible to assess accurately their overdensities or kinematics, and thereby their masses. To date, there have only been a handful of $z \gtrsim 3$ protoclusters with $\gtrsim 10$ spectroscopically confirmed members (e.g., Steidel et al. 1998; Miller et al. 2018; Long et al. 2020). Enlarging this sample is therefore critical to understanding the evolution of overdense environments in the first 2 Gyr of the Universe.

Deep and unbiased spectroscopic surveys, like those conducted on nearby clusters, are generally too expensive to complete over large volumes at the high redshifts of protoclusters. Instead of using blank-field surveys, many protoclusters are identified by surveying the areas around rare, massive galaxies, such as dusty star-forming galaxies (DSFGs; e.g., Casey 2016) or AGNs (e.g., Ivison et al. 2000). Some protoclusters contain multiple DSFGs with individual SFRs $\gtrsim 100~{\rm M}_{\odot}~{\rm yr}^{-1}$ within volumes of only a few hundred cMpc³ (e.g., Miller et al. 2018; Long et al. 2020; Wang et al. 2021). These protocluster "cores" are the most densely star-forming extended structures in the Universe.

Using 2 mm and 3 mm linescans with the Northern Extended Millimeter Array (NOEMA), Jones et al. (2021) obtained CO spectroscopic redshifts (speczs) of three ultra-bright ($S_{850\mu\mathrm{m}} \geq 11~\mathrm{mJy}$) DSFGs at the very edge of the SCUBA-2 coverage of the GOODS-N. Two of the three were at $z\sim3.14$ (red squares in Figure 1) and separated by only 2.7′, or 5.0 cMpc at z=3.14. Jones et al. (2021) surmised that these DSFGs may trace a mas-

sively star-forming protocluster at this redshift. However, due to their rarity, DSFGs are very biased tracers of mass (Miller et al. 2015). Thus, confirming and characterizing a protocluster requires additional spectroscopic observations of other candidate protocluster members.

In this work, we present our spectroscopic surveys of galaxies near the $z \sim 3.14$ DSFGs from Jones et al. (2021). In Section 2, we describe our NOEMA observations of a further three SCUBA-2 sources (Section 2.1), as well as our Keck/LRIS and Keck/MOSFIRE observations of "normal" star-forming galaxies (Section 2.2). In Section 3, we present the results of these observations, including the detection of two $z \sim 3.1$ structures. In Section 4, we calculate the overdensities of these two structures and show that they will likely reach z = 0masses of $M_{\rm tot} \gtrsim 5 \times 10^{14} {\rm M}_{\odot}$. In Section 5, we discuss the likely future of these overdensities and show that they are likely to combine to form a single cluster by z = 0, and in Section 6, we note the existence of a dust-rich protocluster core in the z = 3.14 substructure. Finally, we summarize our work in Section 7.

We assume a concordance flat $\Lambda \mathrm{CDM}$ cosmology with $H_0 = 70~\mathrm{km~s^{-1}~Mpc^{-1}},~\Omega_{\mathrm{m},0} = 0.3,~\mathrm{and}~\Omega_{\Lambda} = 0.7$ throughout this work. All magnitudes are in the AB magnitude system.

2. SPECTROSCOPIC DATA

2.1. NOEMA

The spatial resolution of SCUBA-2 is too poor to determine accurately optical/near-infrared (NIR) counterparts to submillimeter (submm) sources. Instead, interferometric observations are necessary to obtain the positions and speczs of the DSFGs. Jones et al. (2021) confirmed that two DSFGs in the neighborhood of the GOODS-N (GN-CL-2 and GN-CL-3; see Table 1) have redshifts of z = 3.133 and z = 3.150, respectively, based on their CO(5-4) and CO(3-2) lines. With a target redshift of $z \sim 3.14$, we observed with NOEMA (Project Code W20DH, P.I. L. Jones) the next three brightest SCUBA-2 sources in the field (GN-CL-4, GN-CL-5, and GN-CL-6). We observed in two tunings, with Local Oscillator (LO) frequencies of 90 and 145 GHz, to target the CO(3-2) and CO(5-4) lines, respectively, in the lower sideband (LSB) of each tuning. The LO frequencies of NOEMA tunings are at the center of a 7.744 GHz gap between two 7.744 GHz sidebands, so LSBs of the band 1 and band 2 tunings cover 78.384 - 86.128 GHz and 133.184 - 141.128 GHz, respectively. These correspond to CO(3-2) at z = 3.02 - 3.41 and CO(5-4) at z = 3.08 - 3.32. In addition to these new data, we retrieved archival NOEMA observations of GN-CL-2 in

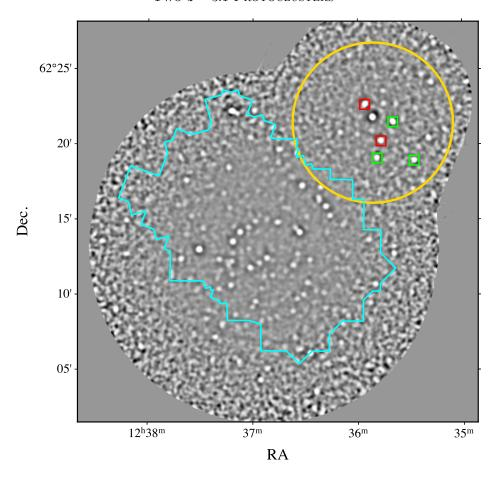


Figure 1. SCUBA-2 850 μ m map of the GOODS-N from SUPER GOODS (Cowie et al. 2017; Jones et al. 2021). The HST/WFC3 F160W footprint of CANDELS (Grogin et al. 2011), which roughly corresponds to the regions covered by the Barger et al. (2008), DEEP3 (Cooper et al. 2011), 3D-HST (Brammer et al. 2012), and MOSDEF (Kriek et al. 2015) spectroscopic surveys, is marked in cyan. The two $z \sim 3.14$ DSFGs from Jones et al. (2021) are marked by the red squares, and the gold circle is a 10 cMpc (5.4') radius circle around the average position of those DSFGs, which is where we conducted our Keck observations. The three NOEMA targets described in Section 2.1 are marked by the green squares.

the 3 mm band from Project S19CV (P.I.s A. Weiß and S. Chapman), which cover the frequency of the expected ${\rm CO}(3-2)$ line.

All the NOEMA data were taken in the compact D-configuration to obtain total line fluxes. Beam sizes were approximately $1.9'' \times 3.6''$ at 3 mm and $1.4'' \times 2.0''$ at 2 mm in the 10D configuration, and $4'' \times 7''$ at 3 mm and $2.5'' \times 3''$ at 2 mm in the older 9D configuration. These data were reduced using the standard pipeline in GILDAS with the default data quality parameters, yielding a typical phase rms of $\sim 10-30$ degrees. A more detailed description of the calibration and imaging of these NOEMA data will be available in a companion paper (M. Nicandro Rosenthal et al. 2024, in prep.), where we will discuss the physical properties of the galaxies in our sample.

We list the SCUBA-2 sources that we observed with NOEMA in Table 1.

2.2. Keck Multi-Object Spectroscopy

In addition to massive and rare galaxies like DSFGs, protoclusters have many tens of less massive members, i.e., "normal" star-forming galaxies, which can be detected with optical and/or NIR spectroscopy. There have been many spectroscopic surveys of the GOODS-N (e.g., Barger et al. 2008; Cooper et al. 2011; Brammer et al. 2012; Kriek et al. 2015), but these surveys targeted the original GOODS (Giavalisco et al. 2004) or CANDELS (Grogin et al. 2011) HST fields (cyan outline in Figure 1). They do not cover the region around the $z\sim3.14$ DSFGs discovered by Jones et al. (2021) (red squares in Figure 1).

We therefore conducted a new Keck spectroscopic survey northwest of the original GOODS-N field. Using the ground-based and Spitzer/IRAC catalog of Hsu et al. (2019), we targeted optical/NIR-selected galaxies with photometric redshifts (photzs) $z_{\rm phot} \sim 3$. This region

GN-CL-5

GN-CL-6

63299

89441

188.86538

188.95347

62.31574

62.31800

Hsu ID RA**FWHM** Name Dec $S_{850\mu m}^{a}$ Project Transition $\nu_{
m obs}$ $z_{
m spec}$ [deg] [deg][mJy][GHz] $[\mathrm{km \ s}^{-1}]$ Protocluster Members GN-CL-2 77630 188.98283 62.37750 11.7 ± 0.5 W19DG CO(5-4)138.84 3.1504 405 ± 26 S19CV CO(3-2) 490 ± 77 83.30 3.1513 GN-CL-3 85384 188.94433 62.33703 11.5 ± 0.6 W19DG CO(5-4)139.44 3.1326 575 ± 48 W19DG CO(3-2)83.663.1332 527 ± 46 GN-CL-4N 81640 188.91755 62.35860 3.6 ± 0.5 W20DHCO(5-4)139.263.1381 798 ± 111 W20DHCO(3-2) 326 ± 81 83.513.1410 CO(5-4) 675 ± 119 GN-CL-4S 188.91571 62.35784 4.5 ± 0.5 W20DH 139.23 3.1390 W20DH CO(3-2)83.543.1392 537 ± 193 Other NOEMA Detections

Table 1. NOEMA Line Detections

 $a-850~\mu{\rm m}$ fluxes are total fluxes from SCUBA-2 (Cowie et al. 2017), except for those of GN-CL-4N and GN-CL-4S, which are from SMA (M. Nicandro Rosenthal et al. 2024, in prep.). The total flux of GN-CL-4 from SCUBA-2 is $10.8\pm0.5~{\rm mJy}$. $b-{\rm GN-CL-4S}$ is undetected in ground-based and HST optical-to-NIR imaging (M. Nicandro Rosenthal et al. 2024, in prep.). $c-{\rm Only}$ one emission line is detected. The stated redshifts assume the detected line is a CO emission line and use the solution closest to the photzs from Hsu et al. (2019).

W20DH

W20DH

 $CO(4-3)^{c}$

 $CO(6-5)^{c}$

98.96

153.66

 $3.6588^{\ c}$

 $3.5000^{\ c}$

 619 ± 57

 843 ± 130

 8.6 ± 0.8

 8.2 ± 0.6

	LRIS			MOSFIRE					
(1)	(2)	(3)	(4)	(5)	(6)	(7)	(8)	(9)	
Type	$N_{ m obs}$	$N_{ m det}$	$f_{ m det}$	$N_{ m obs}$	$N_{ m det}$	$f_{ m det}$	$f_{\mathrm{det}}^{(K \leq 23)}$	$f_{\text{det}}^{(K>23)}$	
smm	4	2	50.0%	23	6	26.1%	4/11 = 36.4%	2/12 = 16.7%	
z3a	45	9	20.0%	141	67	47.5%	15/28 = 53.6%	52/113 = 46.0%	
z3b	25	5	20.0%	140	37	26.4%	5/20 = 25.0%	32/120 = 26.7%	
Total main targets	74	16	21.6%	304	110	36.2%	24/59 = 40.7%	86/245 = 35.1%	
cont	24	3	12.5%	_	_	_	_	_	
$20 \mathrm{cm}$	7	0	0.0%	_	_	_	_	_	
hiz	30	2	6.67%		_	_	_		
z2	_	_	_	85	23	27.1%	10/28 = 35.7%	13/57 = 22.8%	
Total filler targets	62	5	8.1%	85	23	27.1%	10/28 = 35.7%	13/57 = 22.8%	
Grand total	136	21	15.4%	389	133	34.2%	34/87 - 39.0%	99/302 - 32.8%	

Table 2. Keck Targets and Detection Fractions

covers the overdensity of $z_{\rm phot} \sim 3.1$ Lyman Break Galaxies (LBGs) identified by Jones et al. (2021). We prioritized optical/NIR sources within 5" of the centroid of an 850 μ m source ("smm" in Table 2), which might be counterparts to the 850 μ m source, then sources with $3.0 \leq z_{\rm phot} \leq 3.3$ ("z3a"), and finally sources with $2.7 \leq z_{\rm phot} < 3.0$ or $3.3 < z_{\rm phot} \leq 3.6$ ("z3b"). In addition to these main science targets, we included filler objects to maximize the number of slits per mask (see Sections 2.2.1 and 2.2.2). In Table 2, we give the number of galaxies of each type that we observed and detected with LRIS and MOSFIRE.

2.2.1. *LRIS*

We conducted one night of observations with the Low-Resolution Imaging Spectrometer (LRIS; Oke et al. 1995) on March 27, 2022. For these observations we used the 5600 Å dichroic, with the 600/4000 grism on the blue side of LRIS to target Ly α emission at $\lambda_{\rm obs} \approx 5000$ Å, and the 400/8500 grating on the red side with a central wavelength of 8500 Å to target UV absorption features. We imposed a magnitude limit of $V \leq 25.2$ for our LRIS targets. We observed each slitmask for 3×1800 s on the blue side and 6×900 s on the red side, for a total of 90 minutes per mask (the red side

requires shorter exposures to minimize the impact of cosmic rays on its thicker CCD). We reduced these data with an in-house IDL package to apply all calibrations, including sky subtraction, flat fielding, bias correction, and wavelength calibration. For details, we refer the reader to Section 2 of Cowie et al. (1996) and Section 2 of Cowie et al. (2004).

For LRIS filler objects, we targeted radio sources detected in the 1.4 GHz Karl G. Jansky Very Large Array (VLA) mosaics from Morrison et al. (2010) and Owen (2018) ("20cm"), and candidate high-redshift sources with $z_{\rm phot} > 2.5$ ("hiz"). In each mask, we also included several bright V-band continuum objects ("cont") to aid in our reductions.

2.2.2. MOSFIRE

We also observed with the Multi-Object Spectrometer For Infra-Red Exploration (MOSFIRE; McLean et al. 2010, 2012) over a total of four nights, on March 17-18, 2021 and March 25-26, 2022. We used K-band multi-object spectroscopy to target the [O III] $\lambda\lambda 4959,5007$ Å doublet at $3.03 \le z \le 3.59$ ($\lambda_{\rm obs} = 2.0 - 2.3~\mu{\rm m}$). We imposed a magnitude limit of $K_s \le 24.5$ on the large majority of our MOSFIRE targets, with four exceptions, which we included when additional $K_s \le 24.5$ objects could not be fit on a mask. Of these, only one was detected, at z = 3.3198. This redshift is sufficiently high that it does not affect our overdensity analysis in Section 4.

We observed each slitmask for 5 repeats of an ABBA dither pattern with 180 s exposures, giving a total of 1 hr of exposure time per mask. As with the LRIS data, we reduced these MOSFIRE data using our own IDL package, the details of which are discussed in Section 2.4 of Cowie et al. (2016).

For MOSFIRE filler objects, we observed sources with 1.9 < $z_{\rm phot}$ < 2.7 ("z2"), targeting the [N II] $\lambda\lambda6549,6585\,\text{Å} + \text{H}\alpha$ complex in the K-band at $2.04 \le z \le 2.50$.

2.2.3. Completeness

As a rough estimate of our completeness, we consider how many galaxies that satisfy our "z3a" and "z3b" criteria within a circle of radius 10 cMpc around the average position of GN-CL-2 and GN-CL-3 we observed. We selected this radius because simulated and observed protoclusters have been shown to contain most of their galaxies and mass within ~ 10 cMpc (e.g., Chiang et al. 2013; Casey 2016; Alberts & Noble 2022). This corresponds to an angular radius of 5.4' at z=3.1 (yellow circle in Figure 1). Within this circle, we observed 100/127 (78.7%) of "z3a" and 142/258 (55.0%) of "z3b"

galaxies that satisfied either our $K_s \leq 24.5$ or $V \leq 25.2$ magnitude limit.

3. RESULTS

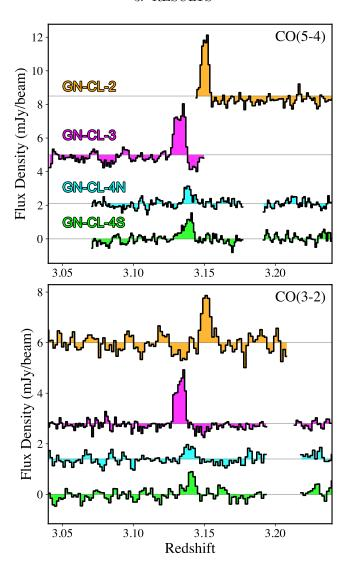


Figure 2. NOEMA CO(5–4) and CO(3–2) spectra of the four DSFGs at $z=3.143\pm0.01$. From top to bottom the spectra are for GN-CL-2, GN-CL-3, GN-CL-4N, and GN-CL-4S. The spectra have been Gaussian smoothed and arbitrary flux offsets were added for display purposes.

3.1. NOEMA CO Detections

We detected at least one strong CO line in each of the three SCUBA-2 sources we observed as part of NOEMA Project W20DH. As described in the following paragraphs, these detections were sufficient to confirm or rule out the galaxies' protocluster membership. Following the procedure in Jones et al. (2021), we generated a one-dimensional (1D) spectrum from the brightest con-

tinuum spaxel in the NOEMA image cube for each sideband, and we inspected these by hand for possible emission lines. In Figure 2, we show the CO(5–4) and CO(3–2) spectra of the four DSFGs with line emission detected in this way (e.g., GN-CL-2, GN-CL-3, GN-CL-4N, and GN-CL-4S). To measure line widths and redshifts, we fit single Gaussians to the 1D spectra. We give the results of this fitting procedure in Table 1, and we describe the individual sources below:

GN-CL-2 (archival)—This source was already found to have a 4.3 mJy line centered at 138.9 GHz by Jones et al. (2021). Those authors used the March 2021 MOSFIRE observations presented in this paper to confirm that this source had $z_{\rm spec}=3.150$, which shows that this line is CO(5–4). We inspected the archival 3 mm observations of GN-CL-2 and measured a CO(3–2) line at the same redshift.

GN-CL-3 (archival)—Like GN-CL-2, GN-CL-3 was originally discussed in Jones et al. (2021), but we summarize their results here for completeness. Jones et al. (2021) identified two bright lines in the NOEMA spectra of GN-CL-3, centered at 139.5 and 83.7 GHz. These lines are consistent with CO(5–4) and CO(3–2), respectively, at a redshift of z=3.133.

GN-CL-4—This source is resolved by NOEMA into two component galaxies separated by 7". In both of these components, we detected strong line emission in the 2 mm and 3 mm NOEMA spectra. Based on their sky frequencies, we find that these lines are CO(5–4) and CO(3–2) at $z_{\rm spec}=3.139.$

GN-CL-5—We measure a single strong line in GN-CL-5 at 99.0 GHz, which is consistent with either CO(2–1) at z=1.330 or CO(4–3) at z=3.659. All other CO lines at $1 \le z \le 8$ are ruled out by the non-detection of additional lines in our spectral coverage. The NOEMA source is coincident with a galaxy with $z_{\rm phot}=3.33\pm1.12$, favoring CO(4–3) at z=3.659.

GN-CL-6—We detect one strong line in GN-CL-6 at 153.7 GHz, which is inconsistent with $z\sim3.1$. Of the many possible redshift solutions for GN-CL-6, two are ruled out: CO(7–6) at z=4.240 is ruled out by the lack of a [C I]($^3\mathrm{P}_2$ – $^3\mathrm{P}_1$) line, and CO(8–7) is ruled out by the lack of additional CO lines at lower frequencies. The line emission is coincident with a $z_{\mathrm{phot}}=4.300$ galaxy from Hsu et al. (2019). GN-CL-6 has a 450 $\mu\mathrm{m}/850\,\mu\mathrm{m}$ flux ratio of ≈ 2.2, whereas most $z\sim1$ DSFGs have ratios of ≥ 3 (Barger et al. 2022; Cowie et al. 2022), suggesting that it lies at $z\gtrsim2$. We therefore find the line is most likely CO(6–5) at z=3.5000.

3.2. Keck Spectroscopic Detections

We detected a total of 24/138 of our LRIS targets (17.4%) and 132/385 of our MOSFIRE targets (34.3%), including 2 galaxies that we detected with both instruments, one of which is GN-CL-2. This yields a total of 154 new speczs from Keck. In Table 3, we give their positions, magnitudes, and redshifts.

As we show in Figure 3, we obtained the highest detection rate in galaxies with $z_{\rm phot} \sim 3.1$, where the [OIII]+H β complex is detectable in K-band spectroscopy. We find a total of 78 galaxies have $3.0 \leq z_{\rm spec} \leq 3.3$. Overall, 89.2% of our detections have normalized absolute redshift deviations $|z_{\rm spec}-z_{\rm phot}|/(1+z_{\rm spec}) \leq 0.15$, with a normalized median absolute deviation $\sigma_{\rm NMAD}=0.042$, which is consistent with expectation for z>1 sources from Hsu et al. (2019). We give the number of observed and detected galaxies for each selection type in Table 2.

As listed in Table 2, we had 69 "z3a" targets that we detected with either LRIS or MOSFIRE. Of these, 47 (68.1%) had $3.0 \le z_{\rm spec} \le 3.3$. We also had 44 "z3b" detections, of which 23 (52.3%) had $3.0 \le z_{\rm spec} \le 3.3$ and a further 11 (25.0%) had other redshifts between $2.7 \le z_{\rm spec} \le 3.6$. In addition to the NOEMA linescans of the brightest SCUBA-2 sources, we also detected a total of 10 "smm" targets: 2/4 targeted with LRIS and 9/26 targeted with MOSFIRE. Both of these counts include GN-CL-2, which was detected with all three instruments (including NOEMA). GN-CL-3 was also detected with MOSFIRE. Apart from the NOEMAdetected DSFGs detailed in Section 3.1, none of the "smm" detections have speczs similar to those of the other DSFGs. Thus, while we give their positions and redshifts in Table 3, we do not include them in our analysis for the remainder of this work.

3.3. Redshift Spikes

We show the histogram of all speczs in our survey in the top panel of Figure 4 with bins of $\Delta z = 0.02$, which corresponds to a co-moving depth of $d_{\rm c} \sim 18\,{\rm cMpc}$ at $z \sim 3$. This binning was chosen such that the co-moving depth is similar to the size of our survey area (the 10 cMpc radius circle in Figure 1). The redshift histogram includes two "spikes", reminiscent of previous spectroscopic confirmations of protoclusters (e.g., Steidel et al. 1998; Chapman et al. 2009), which contain 16 and 14 galaxies at z=3.13-3.16 and z=3.09-3.11, respectively. Henceforth, we will refer to these as GNCL-z3.14 and GNCL-z3.10, respectively. We note that while the bin width here does maximimze the contrast of the spikes, we do not calculate the galaxy overdensity directly from these spikes (we describe our actual method-

(1)	(2)	(3)	(4)	(5)	(6)	(7)	(8)	(9)	(10)	(11)
Type	Hsu ID	RA	Dec.	V	R	K_s	$z_{ m phot}$	$z_{ m opt}$ a	$z_{ m NIR}^{b}$	$z_{\rm CO}$ c
		[deg]	[deg]	[AB]	[AB]	[AB]				
smm	_	188.91560	62.3569	_	_	_	_	-3.0	-3.0	3.139
z3a	80570	188.89441	62.3621	25.27	25.18	23.94	3.1831	-3.0	3.1438	-3.0
z3a	79176	188.90288	62.3703	25.22	24.76	24.17	3.1209	-3.0	3.1344	-3.0
z3b	79100	188.93536	62.3724	24.94	24.73	23.20	3.4462	-3.0	3.1388	-3.0
z3b	78192	188.79875	62.3750	26.79	25.67	21.98	3.3747	-3.0	3.1485	-3.0
z3b	76939	188.97598	62.3792	24.99	24.67	24.09	3.3360	-3.0	3.1428	-3.0
z3a	76454	188.97029	62.3839	24.67	24.76	23.02	3.1756	-3.0	3.1431	-3.0
smm	81640	188.91751	62.3586	28.38	26.45	22.47	3.4000	-3.0	-1.0	3.139
z3b	76319	188.97017	62.3744	24.31	23.49	22.26	3.3299	-3.0	3.1429	-3.0
z3a	68202	189.19633	62.4396	25.54	25.52	23.64	3.0964	-3.0	3.151	-3.0

Table 3. Spectroscopic Detections from our NOEMA and Keck Surveys

Columns are (1) Object type (Section 2.2); (2)–(4) sequence number, right ascension, and declination from Hsu et al. (2019), where available; otherwise, the positions are from NOEMA (this work); (5)–(8) V-band, R-band, and K_s -band magnitude and photz from Hsu et al. (2019); (9)–(11) specz from LRIS, MOSFIRE, and NOEMA. For all speczs, positive values are measurements, -1.0 are non-detections with that instrument, and -3.0 were not observed with that instrument. The complete table is available in machine readable form in the online version.

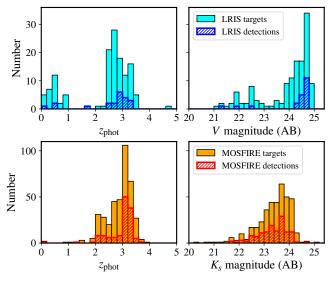


Figure 3. Histograms of the photzs and broadband magnitudes of our targets (filled bars) and detections (hatched bars). Top: LRIS observations and detections, which were selected with a limiting magnitude of $V \leq 25.2$. Bottom: MOSFIRE observations and detections, which were selected with a limiting magnitude of $K_s \leq 24.5$. The bottom-left panel shows a higher MOSFIRE detection fraction for galaxies with $z_{\rm phot} \sim 3$, which reflects the detectability of the [OIII] and ${\rm H}\beta$ complex in the K-band at these redshifts.

ology in Section 4). In the bottom panel of Figure 4, we show a zoom-in of the histogram with a binning of $\Delta z = 0.005 \ (\Delta d_c \sim 4.5 \, \mathrm{cMpc}).$

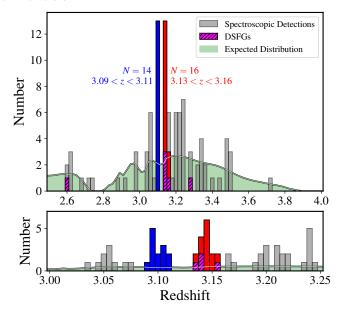


Figure 4. Top: Histogram of speczs from our combined NOEMA and Keck surveys. The green region in the background shows the expected number of galaxies per $\Delta z = 0.02$ bin based on our photz selection (see Appendix A). The red and blue colored bars indicate GNCL-z3.14 and GNCL-z3.10, respectively (see Section 4). Hatched magneta bars indicate DSFGs with speczs from our survey. Bottom: The same histogram, but with bins of $\Delta z = 0.005$ and zoomed in.

The higher-redshift spike, GNCL-z3.14, contains 4 DSFGs, which are denoted by the hatched magenta bars in Figure 4. Meanwhile, GNCL-z3.10 has no confirmed DSFGs. The number of galaxies per bin and the volume

corresponding to each bin are similar to the z=3.09 SSA22 protocluster from Steidel et al. (1998), but we detect two overdensities in close proximity.

4. TWO GALAXY OVERDENSITIES

Our spectroscopic surveys show two clear overdensities of galaxies at z=3.10 and z=3.14. However, not all high-redshift overdensities eventually collapse into clusters. In this work, we take "protocluster" to mean objects that will collapse into clusters with $M_{z=0} \geq 10^{14} \, \mathrm{M}_{\odot}$ (Chiang et al. 2013; Overzier 2016; Alberts & Noble 2022). In this section, we calculate the precise galaxy overdensities of these spikes and convert them into matter overdensities and total masses. Galaxy and mass overdensities are defined, respectively, as

$$\delta_{\rm gal,obs} \equiv \frac{N_{\rm obs} - N_{\rm exp}}{N_{\rm exp}} \,,$$
 (1)

and

$$\delta_{\rm m} \equiv \frac{\rho_{\rm m} - \bar{\rho}_{\rm m}(z)}{\bar{\rho}_{\rm m}(z)} \,, \tag{2}$$

where $N_{\rm obs}$ is the number of galaxies observed in a given volume, $N_{\rm exp}$ is the number of galaxies expected in that same volume, $\rho_{\rm m}$ is the observed total matter density, and $\bar{\rho}_{\rm m}(z)$ is the average matter density at a given redshift. Following Steidel et al. (1998), galaxy and matter overdensities are related by

$$1 + b \,\delta_{\rm m} = C(1 + \delta_{\rm gal,obs}). \tag{3}$$

Here $C \equiv V_{\rm true}/V_{\rm app}$ is the redshift distortion factor that relates the true volume occupied by the galaxies to the apparent volume based on their minimum and maximum observed redshifts, and b is the linear galaxy bias, which is a dimensionless scalar that depends on the properties of the observed galaxies, as well as the scale on which the overdensity is measured (Chiang et al. 2013). Collapsing structures have C < 1 and virialized structures have C > 1. The subscript "obs" refers to the fact that $\delta_{\rm gal,obs}$ is measured for an apparent volume without correcting for the redshift distortion. From Lahav et al. (1991), the redshift distortion factor and mass overdensity are related by

$$C = 1 + f - f(1 + \delta_{\rm m})^{1/3},$$
 (4)

where $f = \Omega_{\rm m}(z)^{4/7}$. For $z \sim 3.1$, $f \sim 0.98$. By simultaneously solving Equations 3 and 4 with fixed values of b and $\delta_{\rm gal,obs}$, it is straightforward to solve for C and $\delta_{\rm m}$.

For each of the spikes described in Section 3, we measure the overdensity in a cylindrical volume. The depth of the cylinder is defined by the lowest and highest redshift galaxies in each group, and we take the radius of

the cylinder to be 8 cMpc (4.3' at z=3.1), which is the typical effective radius of the most massive $z\sim 3$ protoclusters (e.g., Chiang et al. 2013). Using this definition, we obtain apparent volumes of $V_{\rm app}^{({\rm z}3.14)}=4030~{\rm cMpc}^3$ and $V_{\rm app}^{({\rm z}3.10)}=3310~{\rm cMpc}^3$. We show the boundaries of volumes A and B in red and blue, respectively, in Figure 5. Measuring $N_{\rm obs}$ is then as simple as counting the number of spectroscopically confirmed galaxies within each of these volumes. To calculate $N_{\rm exp}$, we use two methods: one by photz selection, and one by comparing to broadband luminosity functions at $z\sim 3$.

4.1. Comparison to Photometric Redshifts

To estimate the galaxy overdensities of the two redshift spikes, we take advantage of the fact that all but two¹ of our targets have eazy (Brammer et al. 2008) photzs from Hsu et al. (2019). Hsu et al. (2019) tested their photz fits against a subset of their sample that already had good speczs. If we assume that our targets follow the same distribution in $(z_{\rm spec}-z_{\rm phot})/(1+z_{\rm phot})$ as these, then for any given input photz, we can calculate a probability distribution function (PDF) of the true redshift. We take $P(z_{\rm min} \leq z \leq z_{\rm max})$ to be the integral of this PDF over some redshift bounds. We take the probability of detecting each galaxy to be the product of this probability and the estimated detection fraction for galaxies in a given photz range. We describe these calculations in detail in Appendix A.

Using this method, we expect a total of $N_{\rm exp}=1.97$ galaxies in GNCL-z3.14 and 1.49 galaxies in GNCL-z3.10. From Equation 1, this gives galaxy overdensities of $\delta_{\rm gal,obs}^{(z3.14)}=6.10$ and $\delta_{\rm gal,obs}^{(z3.10)}=7.07$. These overdensity estimates are not corrected for the fact that there were a greater than expected number of $z_{\rm phot}\sim3.1$ galaxies in our survey area to begin with, as first identified by Jones et al. (2021), and may therefore be considered lower limits.

4.2. Comparison to Broadband Luminosity Functions

To obtain the most direct estimate of $N_{\rm exp}$, we take the number density of field galaxies selected similarly to those in our spectroscopic survey and multiply by the observed volume. We use the K-band luminosity function (LF) of Mortlock et al. (2017), since we observed the majority of our targets with MOSFIRE using a K-band magnitude cut. In Figure 6, we show that in all bins of $K \leq 24.5$, we detect more galaxies than would be expected for the co-eval field. To estimate the total value

 $^{^1}$ GN-CL-1 was not included due to its proximity to a bright star, and GN-CL-4S is optically dark and therefore does not have a Hsu et al. (2019) ID.

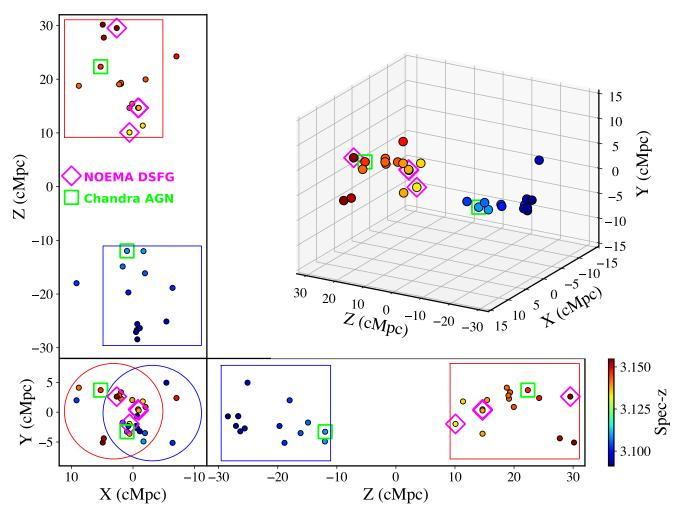


Figure 5. Top right: A 3D map of the protoclusters. Left, bottom-left, and bottom: 2D projections of the same region. In all panels, the radial offsets (Z) in physical units are calculated assuming no peculiar velocities. Magenta diamonds indicate NOEMA-detected DSFGs, and green squares indicate Chandra-detected AGNs. The red and blue outlines are the projected boundaries of the volumes used to calculate the overdensities of GNCL-z3.14 and GNCL-z3.10, respectively.

of $N_{\rm exp}$, we summed all the bins with $K \leq 24.5$ mag multiplied by the width of the bins, i.e., 0.5 mag, and by the overall detection fraction of our MOSFIRE survey. For 2.75 < z < 3.75, Mortlock et al. (2017) find a typical source density of $n_{\rm gal} = 3.53$ cMpc⁻³ for galaxies with $M_K \leq -22.5$ ($K \leq 24.62$ at z = 3.1). Based on this, we find $N_{\rm exp}^{(z3.14)} = 1.29$ and $N_{\rm exp}^{(z3.10)} = 1.17$, which correspond to observed galaxy overdensities of $\delta_{\rm gal,obs}^{(z3.14)} = 9.10$ and $\delta_{\rm gal,obs}^{(z3.10)} = 9.28$. Note that for these calculations, we use $N_{\rm obs}^{(z3.14)} = 13$ rather than 14, as GN-CL-4S is not detected in the K-band, and hence it must be excluded from the comparison to the K-band LF.

4.3. Mass Overdensities and Total Masses

Having calculated $\delta_{\rm gal,obs}$, we can now obtain the matter overdensity $\delta_{\rm m}$ for each protocluster by simultaneously solving Equations 3 and 4. We assume a bias

of b=2.71, which is appropriate for $M_{\star}>10^{10}~{\rm M}_{\odot}$ galaxies at $z\sim 3$ measured over a 15 cMpc³ volume (Chiang et al. 2013), since $V_{\rm app}^{(z3.14)}\sim V_{\rm app}^{(z3.10)}\sim (15~{\rm cMpc})^3=3375~{\rm cMpc}^3$. We measure redshift distortions of $C\approx 0.6-0.7$ for both GNCL-z3.14 and GNCL-z3.10 using both of our overdensity calculation methods, finding slightly higher distortions for the photozbased estimates. We also measure matter overdensities of $\delta_{\rm m}>1$ for both of these methods, finding slightly higher matter overdensities for the LF-based estimates. We list the specific values in Table 4. Following Steidel et al. (1998), we convert these values into a redshift zero total mass using the formula

$$M_{z=0} = C V_{\text{app}} \bar{\rho}_{\text{m}} \left(1 + \delta_{\text{m}} \right), \tag{5}$$

where $\bar{\rho}_{\rm m} = 4.08 \times 10^{10} {\rm M}_{\odot} {\rm cMpc}^{-3}$ at z = 3.10. This gives $M_{z=0} \simeq (6-7) \times 10^{14} {\rm M}_{\odot}$ for both protoclusters using both methods. Again, we list the specific masses

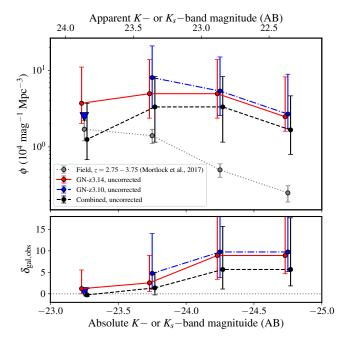


Figure 6. Top: K_s -band LFs of GNCL-z3.10 (blue), GNCL-z3.14 (red), and the combined potential hyperprotocluster (black; see Section 5) compared with the z=2.75-3.75 field K-band LF of Mortlock et al. (2017) (gray). The LFs for the protoclusters in this work are not corrected for completeness; thus, the actual number densities within the protoclusters may be higher. Bottom: Overdensities of the protoclusters relative to the Mortlock et al. (2017) LF in each bin. The brighter bins are likely more accurate, as our detection fraction and completeness for the fainter bins are substantially lower.

in Table 4. We note, however, that these overdensities, and thus mass calculations, are subject to uncertainties, both in the number of expected galaxies and in the Poisson uncertainty in our number counts. We describe these uncertainties, and the resulting uncertainties in the final masses, in Section 4.5.

4.4. Redshift of Collapse

We showed in Section 4.3 that both overdensities have projected final masses $M_{z=0} \geq 10^{14} \ \mathrm{M}_{\odot}$. To be protoclusters, each overdensity must also collapse and virialize by z=0. We estimate the redshift of collapse analytically using the linear theory of density perturbation growth: we take the redshift of collapse, z_c , to be the redshift at which δ_{L} exceeds the critical density, $\delta_c \simeq 1.686$, as has been demonstrated for several recently-detected $z \sim 2-3$ protoclusters (e.g., Cucciati et al. 2018; Polletta et al. 2021).

We calculate the linear overdensity $\delta_{\rm L}$ at the redshift of our overdensities as a function of $\delta_{\rm m}$ using the approximation in Mo & White (1996) Equation 18. We use Equation 7 from Cucciati et al. (2018) to estimate

Table 4. Measured Properties of the $z \sim 3.1$ Protoclusters

	GNCL-z3.14	GNCL-z3.10	Combined				
$z_{ m min}$	3.133	3.090	3.090				
$z_{ m max}$	3.155	3.110	3.155				
RA [deg.]	188.99307	188.87337	188.93321				
Dec. [deg.]	62.35593	62.35292	62.35444				
$N_{ m specz}$	14	12	25				
$V_{\rm app} \ [{ m cMpc}^3]$	4030	3310	11800				
Photometric Redshift Method (Section 4.1)							
$N_{\rm exp}$	1.97	1.49	5.69				
$\delta_{ m gal,obs}$	6.10	7.07	3.39				
C	0.670	0.642	0.770				
$V_{\rm true} \ [{ m cMpc}^3]$	6570	5800	15600				
$\delta_{ m m}$	1.39	1.54	0.88				
$M_{z=0} [10^{14} \mathrm{M}_{\odot}]$	6.40	6.02	12.0				
$\delta_{\rm L}(z=0)$	2.24	2.34	1.73				
z_c	0.53	0.61	0.05				
Luminos	ity Function M	ethod (Section	4.2)				
$N_{\rm exp}$	1.29	1.17	6.63				
$\delta_{ m gal,obs}$	9.10	9.28	5.08				
C	0.592	0.588	0.703				
$V_{\rm true} \ [{ m cMpc}^3]$	6170	5630	16600				
$\delta_{ m m}$	1.84	1.86	1.21				
$M_{z=0} \ [10^{14} \mathrm{M}_{\odot}]$	7.14	6.57	14.9				
$\delta_{\rm L}(z=0)$	2.56	2.55	2.08				
z_c	0.80	0.79	0.38				
Photometri	c Redshift Mor	te Carlo (Secti	on 4.5)				
$N_{\rm exp}$	$1.87^{+0.94}_{-0.78}$	$1.44^{+0.73}_{-0.68}$	$5.59^{+1.56}_{-1.32}$				
$\delta_{ m gal,obs}$	$6.30^{+5.91}_{-3.01}$	$7.15^{+7.33}_{-3.34}$	$3.44^{+1.62}_{-1.27}$				
C	$0.66^{+0.11}_{-0.13}$	$0.64^{+0.11}_{-0.14}$	$0.77^{+0.06}_{-0.06}$				
$V_{\rm true} \ [{ m cMpc}^3]$	6630^{+1650}_{-950}	5820^{+1630}_{-870}	15600^{+1400}_{-1200}				
$\delta_{ m m}$	$1.42^{+0.80}_{-0.56}$	$1.55^{+0.91}_{-0.59}$	$0.89^{+0.32}_{-0.28}$				
$M_{z=0} \ [10^{14} \mathrm{M}_{\odot}]$	$6.54^{+4.34}_{-2.24}$	$6.07^{+4.54}_{-2.10}$	$12.1^{+3.3}_{-2.6}$				
$\delta_{\rm L}(z=0)$	$2.27^{+0.51}_{-0.56}$	$2.35^{+0.52}_{-0.53}$	$1.74^{+0.33}_{-0.38}$				
z_c	$0.55^{+0.43}_{-0.53}$	$0.62^{+0.43}_{-0.48}$	$0.06^{+0.32}_{-0.46}$				
P_{collapse}	85.2%	89.6%	53.8%				

 $\delta_{\rm L}$ at lower redshifts, to find the redshift z_c at which $\delta_{\rm L}=\delta_c$. For the photz-based overdensity calculations, we measure $z_c=0.53$ in GNCL-z3.14 and $z_c=0.61$ in GNCL-z3.10. This is consistent within our uncertainties (see Section 4.5) with the LF-based estimates of $z_c\approx 0.8$ for both overdensities. This indicates that they are indeed protoclusters and will collapse well before z=0. These values, corresponding to lookback times of 5-7 Gyr, are consistent with the detection of massive, virialized clusters in large Sunyaev-Zeldovich and opticalto-NIR surveys (e.g., Bleem et al. 2015; Balogh et al. 2021).

4.5. Uncertainties and Statistical Significance

To assess the statistical significance of these overdensities, we consider the likelihood that they would be observed and classified as protoclusters (i.e., have measured $M_{z=0} \geq 10^{14}~{\rm M}_{\odot}$), assuming the number of spectroscopic detections per bin follows Poisson statistics. To do so, we ran 1000 Monte Carlo (MC) simulations of the overdensity calculation described in Section 4.1 for each of the two overdensities. Instead of integrating $P(z_{\rm min} \leq z \leq z_{\rm max})$, for each iteration, we generated a random value of z for every galaxy we targeted with Keck, and we summed these to measure a variable $N_{\rm exp}$. We describe this process in greater detail in Appendix A.

For each run, we calculated the associated galaxy and matter overdensities, redshift distortion, redshift of collapse, and z=0 total mass in the same ways as in Sections 4.3–4.4. In Table 4, the quoted uncertainties are from the 16th to 84th percentile of these MC runs. Our MC simulations return 16th to 84th percentile final masses of $M_{z=0}=(4.3-10.9)\times 10^{14}\,\mathrm{M}_{\odot}$ and $M_{z=0}=(4.0-10.6)\times 10^{14}\,\mathrm{M}_{\odot}$ for GNCL-z3.10 and GNCL-z3.14, respectively. We show the histogram of mass outcomes for each of these in Figure 7.

In all 1000 MC simulations for each overdensity, the projected z=0 mass always exceeds $10^{14}~\rm M_{\odot}$. For some simulations with the lowest values of $\delta_{\rm gal,obs}$, we measure $z_c<0$, indicating the overdense structure will not collapse by the present day and therefore cannot be considered bona fide protoclusters. We find that GNCL-z3.14 and GNCL-z3.10 do not collapse by z=0 in 14.8% and 10.4% of our MC simulations, respectively. Once again, because these overdensities were performed using the photzs of our targets to calculate N_{exp} , these calculated likelihoods of collapse by the present day are underestimated. These MC simulations therefore suggest a $\gtrsim 85\%$ likelihood of collapse by z=0.

We caution that this does not mean that GNCL-z3.14 and GNCL-z3.10 will remain separate until z=0. Rather, the more likely scenario is that these two will collapse into substructures of a larger cluster with $M_{z=0}>10^{15}\,{\rm M}_{\odot}$, which we address in Section 5.

5. SUBSTRUCTURES IN A HYPER-PROTOCUSTER

Recent deep spectroscopic surveys have detected socalled hyper-protoclusters: collections of galaxy overdensities and protoclusters in close proximity to each other (e.g., Cucciati et al. 2018). The two overdensities that we have identified in this work are separated by only 42 cMpc, assuming they have negligible peculiar velocities, and so may belong to such a structure. Given their close proximity and high masses, GNCLz3.14 and GNCLz3.10 may be substructures in an extremely massive protocluster that will collapse into a Coma-like ($M>10^{15}~\rm M_{\odot}$) cluster by z=0. We can expect that these structures will collapse into a single halo at some point if the overall overdensity exceeds the critical density $\delta_{\rm L,crit}=1.686$. To test whether this is possible, we repeat the overdensity and mass calculations described in Section 4 using a cylinder of radius 8 cMpc with faces at z=3.09 and z=3.155 and centered on the midpoint on the sky between the two protoclusters' coordinates. This new combined cylinder contains 25 spectroscopically detected galaxies. In Table 4, we give the results.

For both the LF- and the photz-based overdensity methods, we find that this structure will collapse before z=0. We also repeat the MC procedure and measure a matter density of $\delta_{\rm L}(z=0) \geq 1.686$ in 53.8% of runs, with very high projected z=0 cluster masses of $M>10^{15}~{\rm M}_{\odot}$. Furthermore, for the LF method, we calculate a matter overdensity of $\delta_{\rm m}>1$ over co-moving volumes of $>16\,000\,{\rm cMpc}$, which Chiang et al. (2013) find to be consistent with a $>\!80\%$ likelihood of collapse in simulated overdensities.

To check this result, we calculate the likelihood that we have detected the progenitors of two separate clusters separated by 42 cMpc. Galaxy clusters and their progenitors are themselves subject to clustering over large scales (e.g., Peebles 1980; Bahcall & Soneira 1983). This clustering is characterized by the correlation function, $\xi(r) = (r/r_0)^{-1.8}$ (Totsuji & Kihara 1969; Peebles 1980), which is the excess probability of observing two objects (i.e., galaxies or clusters of galaxies) separated by a distance r compared to an unclustered random Poisson distribution.

Given that GNCL-z3.14 and GNCL-z3.10 are the progenitors of either one (if they merge) or two (if they do not) clusters, Bayes' theorem gives the probability that the two overdensities will not merge by z=0:

$$P(2 \mid 1 \text{ or } 2) = \frac{P(2)}{P(1 \text{ or } 2)}.$$
 (6)

where N in each probability P(N) is the number of z=0 clusters that are descendants of the overdensities we detect in our survey volume. We can rewrite this in terms of the Poisson probability and the correlation function:

$$P(2 \mid 1 \text{ or } 2) = \frac{P'(2)[1+\xi(r)]}{P'(1) + P'(2)[1+\xi(r)]}$$
 (7)

where

$$P'(N) = \frac{(nV)^N e^{-nV}}{N!}$$
 (8)

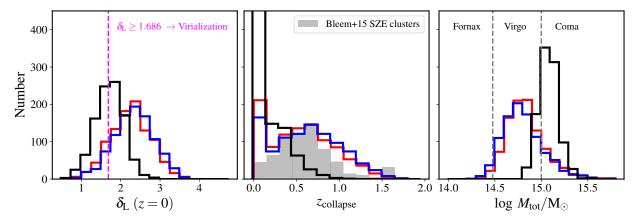


Figure 7. Histograms showing the results of our MC simulations of the protocluster overdensities, as described in Section 4.5 and Appendix B. The red, blue, and black histograms in each panel show the distribution of results for 1000 simulations of GNCL-z3.14, GNCL-z3.10, and the combined group, respectively. Left: Linear overdensity at present day. The magenta dashed line denotes $\delta_L = 1.686$, which is the threshold at which a spherical overdensity virializes. Center: Redshift of collapse, i.e., the redshift at which the linear overdensity crosses the $\delta_L = 0$ threshold. The first bin includes all simulations with $\delta_L(z=0) < 1.686$, i.e., those that do not virialize by the present day. The grey histogram shows the redshift distribution of SPT Sunyaev-Zeldovich Effect-selected clusters from Bleem et al. (2015). Right: Final (z=0) masses of the cluster descendants. The grey lines at $M = 3 \times 10^{14} \,\mathrm{M}_{\odot}$ and $M = 10^{15} \,\mathrm{M}_{\odot}$ indicate the fiducial mass delineations between Fornax-, Virgo-, and Coma-mass clusters in the local universe (e.g., Chiang et al. 2013).

is the Poisson probability of observing exactly N objects within a volume V given a number density of n.

The numerical value of the probability given in Equation 7 depends on the number density n and clustering length r_0 , which differ greatly depending on the richness of the clusters considered. Since for either the single or dual descendant cases, the final masses of the protocluster(s) are very high (> $5 \times 10^{14} \,\mathrm{M}_{\odot}$), we assume $r_0 = 25 h^{-1}$ cMpc and $n = 1.8 \times 10^{-6}$ cMpc, which were found for the richest and most massive clusters in deep SDSS cluster surveys (Bahcall et al. 2003). Taking the volume to be our whole survey volume, roughly $20 \times 20 \times 870 \sim 3.5 \times 10^5 \,\mathrm{cMpc}^3 \ (z = 2.8 - 3.8)$, Equation 7 gives a 34% likelihood of GNCL-z3.10 and GNCLz3.14 being progenitors of two distinct z = 0 clusters. This is likely an overestimation, as we prioritized objects in a narrower redshift range of z = 3.0 - 3.3 in our Keck survey, as noted in Section 2, which would yield a volume of $1.1 \times 10^5 \, \mathrm{cMpc}^3$ and a two-descendant probability of only 14%. We therefore claim an 86% likelihood of the two structures merging.

Because the individual redshifts of collapse of GNCLz3.10 and GNCLz3.14 ($z_c^{z3.10} \sim z_c^{z3.14} \sim 0.5-0.8$) are higher than that of the combined Coma progenitor ($z_c^{\text{combined}} \sim 0.1$ for the photz method and $z_c^{\text{combined}} \sim 0.4$ for the LF method), the descendant of this system may be an interacting/merging cluster or cluster with multiple sub-clusters by $z \sim 0-0.4$. Several such clusters have been observed in this redshift range (e.g., Clowe et al. 2004; Jauzac et al. 2016). Indeed, a recent weak and strong gravitational lensing analysis shows

that the rich z=0.308 cluster Abell 2744 is composed of five mass peaks each with $M_{200}=(1-5)\times 10^{14}\,{\rm M}_{\odot}$ (Cha et al. 2024), similar to the expected final masses of GNCL-z3.14 and GNCL-z3.10.

6. A DUSTY PROTOCLUSTER CORE

While both GNCL-z3.14 and GNCL-z3.10 have similar sizes, galaxy and matter overdensities, and expected total masses (see Section 4), GNCL-z3.14 also has an excess of DSFGs, which may constitute a dusty protocluster "core" with an extremely high SFR density (SFRD), as seen in several other high-redshift protoclusters in the literature (e.g., Miller et al. 2018; Long et al. 2020; Wang et al. 2021). While we leave a full analysis of the physical properties of the protocluster members to an upcoming companion paper (Nicandro Rosenthal et al., in prep.), we estimate the SFRs of the DSFGs belonging to GNCL-z3.14. To do so, we scale a Casey (2012) FIR spectral energy distribution (SED) with a fiducial dust temperature of $T_{\rm dust} = 32\,\rm K$ and emissivity $\beta = 1.8$ to the DSFGs' NOEMA 2 mm continuum fluxes. We then obtain the integrated IR luminosities from these SEDs and convert these to SFRs following a Kennicutt & Evans (2012) law, corrected to a Chabrier (2003) initial mass function. The wavelengths at which we measured the continuum fluxes, integrated luminosities and SFRs inferred from this procedure are given in Table 5. The DSFGs have individual SFRs of 300 to $1000 \text{ M}_{\odot} \text{ yr}^{-1}$, and the total SFR of the four DSFGs is $\Sigma SFR = 2730 \pm 670.$

Table 5. DSFG IR Luminosities and SFRs

Name	$\lambda_{ m obs}$	$S_{2\mathrm{mm}}$	$L_{3-1100\mu m}$	SFR
	[mm]	$[\mu \mathrm{Jy}]$	$[10^{12}L_\odot]$	$[{\rm M}_{\odot}~{\rm yr}^{-1}]$
GN-CL-2	1.895	870 ± 30	9.9 ± 1.0	990 ± 100
GN-CL-3	1.895	900 ± 30	10.3 ± 1.1	1030 ± 110
GN-CL-4N	1.957	320 ± 27	4.0 ± 0.5	400 ± 50
GN-CL-4S	1.957	250 ± 27	3.1 ± 0.5	310 ± 50

GNCL-z3.14 occupies a corrected co-moving volume of $6630^{+1650}_{-950} \, \mathrm{cMpc^3}$. Accounting for only the DSFGs gives a lower limit of SFRD $\geq 0.41^{+0.12}_{-0.14} \, \mathrm{M_{\odot} \ yr^{-1} \ cMpc^{-3}}$. If we instead use the volume of the combined massive protocluster of $15\,600^{+1400}_{-1200} \, \mathrm{cMpc^3}$, we find a lower limit of SFRD $\geq 0.18 \pm 0.05 \, \mathrm{M_{\odot} \ yr^{-1} \ cMpc^{-3}}$. Both of these values are in line with known protoclusters in the literature (see, e.g., Figure 11 of Alberts & Noble 2022, and references therein).

Protocluster cores themselves typically have SFRs of several thousand M_{\odot} yr⁻¹ and occupy only a few hundred cMpc³ (e.g., Miller et al. 2018; Lacaille et al. 2019; Long et al. 2020; Wang et al. 2021). Following these studies, we can define a cylindrical volume around the four DSFGs with a radius of 2.6 cMpc and a depth of 13.3 cMpc, giving a total volume of 280 cMpc³. In such a volume, the SFRD from the DSFGs alone is $9.7 \pm 2.4 \ M_{\odot} \ yr^{-1} \ cMpc^{-3}$. This is also consistent with the densities of protocluster cores in the literature, which have been shown to have SFRDs of $\sim 10-100 \ M_{\odot} \ yr^{-1} \ cMpc^{-3}$ (e.g., Lacaille et al. 2019; Wang et al. 2021; Alberts & Noble 2022).

Interestingly, apart from the presence of these DS-FGs in GNCL-z3.14, both substructures identified in this work have very similar properties. They both extend over a similar sky area, displaying some apparent filamentary structure (as shown in Figure 5), both extend over a redshift range of $\Delta z \approx 0.02$, and both have very similar overdensities and therefore predicted final masses. The fact that no bright DSFGs are observed in GNCL-z3.10 could either be because of a true lack of DSFGs in this substructure, or because the DSFGs within it were too faint to cover with our survey. The former case is addressed by Miller et al. (2015), who find that many of the most dense volumes in the Bolshoi cosmological simulations do not contain DSFGs with $S_{850} > 3 \,\mathrm{mJy}$. While this trend is most pronounced at $z \lesssim 2.5$ where the most massive galaxies have stopped forming stars rapidly due to cosmic downsizing, Miller et al. (2015) note that even at $z \gtrsim 2.5$ the majority of the highest overdensities do not host a DSFG.

Alternatively, there may be DSFGs in GNCL-z3.10 that are fainter than the SCUBA-2 selection for our

NOEMA survey. As described in Table 1, our NOEMA spectroscopic survey includes the six brightest galaxies in the Northwestern extension to the SCUBA-2 coverage of the GOODS-N (see also Figure 1). This rules out the presence of the most highly star-forming Hyper-Luminous Infrared Galaxies (HyLIRGs; $L_{\rm IR} > 10^{13} \, \rm L_{\odot}$) like GN-CL-2 and GN-CL-3 in GNCL-z3.10, but not more moderately luminous DSFGs with $S_{850} = 4$ 6.5 mJy. Calvi et al. (2023) leveraged deep photometric redshift data on the GOODS-N and found that DS-FGs in this field do trace protoclusters, but the DS-FGs occupying these protoclusters had a median $L_{\rm FIR} =$ $4 \times 10^{12} \, \mathrm{L}_{\odot}$, which would correspond to $S_{850} \approx 4 \, \mathrm{mJy}$ at $z \sim 3$ for the dust SED described above. Additionally, deep interferometric observations have shown that some protoclusters have many fainter galaxies down to < 1 mJy that are still FIR-dominated and contribute significantly to the overall SFRD (e.g., Hill et al. 2020).

Whether there are DSFGs in GNCL-z3.10 at a lower brightness or not, the contrast between the two structures warrants a further investigation of the properties of their member galaxies. While the absence of HyLIRGs in GNCL-z3.10 may not imply a difference in the mass distributions of these structures for the reasons stated above, it may indicate some difference in the evolutionary progression of the most massive galaxies in different components of the same larger protocluster, especially considering that there is evidence for correlated triggering of DSFGs in protoclusters (Casey 2016), and at least some DSFGs have very short lifetimes (e.g., Carilli & Walter 2013).

Finally, because massive protoclusters such as the one presented in this work can span up to 30-60 cMpc in the plane of the sky (e.g., Tamura et al. 2009; Cucciati et al. 2018), we inspect the speczs from Hsu et al. (2019) of galaxies to the Southeast of our newly discovered protoclusters (i.e., the CANDELS field) to attempt to identify additional members, and especially additional DSFGs. We particularly aim to take advantage of the fact that Cowie et al. (2017) have SMA positions for many galaxies in their SCUBA-2 sample, which allows us correctly identify NIR counterparts with existing speczs.

We identify 12 further objects with $3.09 \le z_{\rm spec} \le 3.16$ from the Hsu et al. (2019). One of these is the known NIR counterpart of a DSFG. This galaxy, shown by the magenta square in Figure 8, has a specz of $z_{\rm spec} = 3.1465$ and is a more moderately luminous galaxy with $S_{850} = 4.1\,\rm mJy$ (Cowie et al. 2017). We show the positions of all galaxies in this redshift range in the GOODS-N, both with previously measured speczs and those with new speczs from this work, in Figure 8. The galaxies found

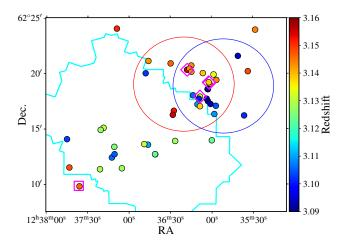


Figure 8. Positions of galaxies with $3.09 \leq z_{\rm spec} \leq 3.16$ in the GOODS-N, including both new speczs from this work and known speczs from the Hsu et al. (2019) catalog. The cyan outline denotes the $HST/{\rm WFC3}$ F160W coverage from CANDELS, and the large unfilled red and blue circles are the same as in the bottom-left panel of Figure 5. The inclusion of existing speczs from Hsu et al. (2019) reveals a possible $z\approx 3.12$ substructure located to the Southeast of the two structures identified in Section 4. The magenta diamonds indicate the $z_{\rm spec}=3.133-3.155$ DSFGs GN-CL-2, 3, 4N, and 4S, and the magenta square shows the SMA position of an additional $z_{\rm spec}=3.1465$ DSFG from Cowie et al. (2017).

to the Southeast are mostly at z = 3.11 - 3.13, lying between the redshifts of the two overdensities.

7. SUMMARY AND CONCLUSIONS

In this work, we presented spectroscopic observations of 507 galaxies just outside of the GOODS-N with the aim of definitively determining the presence or absence of a protocluster at $z\sim3.14$ around two ultra-bright DSFGs. We measured 139 speczs, including NOEMA CO redshifts for four DSFGs, and confirmed the existence of two overdensities at z=3.090-3.110 and z=3.133-3.155, which we refer to as GNCL-z3.10 and GNCL-z3.14, respectively.

We compared the number of spectroscopically confirmed members of each overdensity to the number of galaxies expected from their photzs and from the K-band LF of Mortlock et al. (2017) at $2.75 \leq z < 3.75$. With both methods, we measured galaxy overdensities of $\delta_{\rm gal,obs} \sim 9$ over distortion-corrected volumes of $(5-7)\times 10^3$ cMpc³ for both overdensities. Using the analytical spherical collapse model of Mo & White (1996), we calculated that both overdensities have matter overdensities of $\delta_{\rm m}=1.6-1.9$ and expected z=0 masses similar to that of the Virgo cluster $(M_{\rm tot,z=0}=(6-8)\times 10^{14}~{\rm M}_{\odot})$. We determined that both should collapse and virialize by $z_c\sim 0.5-0.8$.

We used the same overdensity calculation and spherical collapse analysis on a larger volume spanning z=3.09-3.16 and found that the two overdensities combined have a galaxy overdensity of $\delta_{\rm gal,obs}\sim 3-5$ and matter overdensity of $\delta_m\sim 1$. We calculated a >80% likelihood that GNCL-z3.14 and GNCL-z3.10 therefore are substructures in a single protocluster, rather than the progenitors of separate z=0 clusters, and are expected to collapse into a single massive $(M_{tot,z=0}=(1.0-1.5)\times 10^{15}\,{\rm M}_{\odot})$ cluster, with a redshift of collapse of $z_c\sim 0.1-0.4$.

Lastly, while the two protoclusters are very similar in their estimated total masses and overdensities, GNCL-z3.14 contains four DSFGs with a cumulative SFR inferred from their submm emission of Σ SFR = $2730\pm670~{\rm M}_{\odot}~{\rm yr}^{-1}$ contained within a core volume of only 280 cMpc³. These four DSFGs constitute a dusty protocluster core. The position of these two protoclusters just outside of the GOODS-N, in a region with extensive ground- and space-based photometric—and now spectroscopic—observations makes them prime candidates for follow-up investigations of their member galaxies, which may unveil whether there are significant differences in the two groups, and whether these are related to the lack of hyper-luminous DSFGs in GNCL-z3.10.

This work is based on observations carried out under project numbers S19CV, W19DG, and W20DH with the IRAM NOEMA Interferometer. IRAM is supported by INSU/CNRS (France), MPG (Germany) and IGN (Spain). M.J.N.R. and L.H.J. thank their IRAM contacts Vinod Arumugam, Isabella Cortez, and Melanie Krips for their valuable assistance in the reduction of these NOEMA data. We thank the anonymous referee for their helpful feedback.

We gratefully acknowledge support for this research from a Kellett Mid-Career Award and a WARF Named Professorship from the University of Wisconsin-Madison Office of the Vice Chancellor for Research and Graduate Education with funding from the Wisconsin Alumni Research Foundation (A. J. B.), the William F. Vilas Estate (M.J.N.R., A.J.T.), and NASA grant 80NSSC22K0483 (L. L. C.).

Some of the data presented herein were obtained at the W. M. Keck Observatory, which is operated as a scientific partnership among the California Institute of Technology, the University of California and the National Aeronautics and Space Administration. The Observatory was made possible by the generous financial support of the W. M. Keck Foundation.

The James Clerk Maxwell Telescope is operated by the East Asian Observatory on behalf of The National Astronomical Observatory of Japan; Academia Sinica Institute of Astronomy and Astrophysics; the Korea Astronomy and Space Science Institute; the National Astronomical Research Institute of Thailand; Center for Astronomical Mega-Science (as well as the National Key R&D Program of China with No. 2017YFA0402700). Additional funding support is provided by the Science and Technology Facilities Council of the United Kingdom and participating universities and organizations in the United Kingdom and Canada.

The authors wish to recognize and acknowledge the very significant cultural role and reverence that the summit of Maunakea has always had within the indigenous Hawaiian community. We are most fortunate to have the opportunity to conduct observations from this mountain.

Facilities: JCMT (SCUBA-2), NOEMA, Keck (LRIS, MOSFIRE)

Software: astropy (Astropy Collaboration et al. 2013, 2018, 2022), eazy (Brammer et al. 2008), GILDAS (http://www.iram.fr/IRAMFR/GILDAS), IDL (Landsman 1995), matplotlib (Hunter 2007), numpy (Harris et al. 2020), scipy (Virtanen et al. 2020)

APPENDIX

A. CALCULATING N_{EXP} USING OUR PHOTOMETRIC SELECTION

Calculating overdensities requires a calculation of the number of galaxies expected $(N_{\rm exp})$ within a given observed (i.e., not corrected for redshift distortion) volume. We selected our Keck targets based on their photzs from eazy (Brammer et al. 2008), which were compiled by Hsu et al. (2019) based on their UV-to-NIR photometry. Hsu et al. (2019) also compiled speczs for a subset of these galaxies. To calculate $N_{\rm exp}$, we first define a parameter q to be the

difference between the specz and photz of a galaxy, normalized by one plus its photz:

$$q \equiv \frac{z_{\text{spec}} - z_{\text{phot}}}{1 + z_{\text{phot}}} \,. \tag{A1}$$

Because every object in our survey has a fixed photz from Hsu et al. (2019), a PDF of q can be used to draw random values of z_{spec} for each object, simply by inverting the equation above:

$$z_{\text{spec}} = z_{\text{phot}} + q \left(1 + z_{\text{phot}} \right). \tag{A2}$$

While none of our targets had speczs prior to our survey, many objects from the Hsu et al. (2019) sample have both photzs and speczs, and values of q can be calculated for those objects. We use subsamples of these spectroscopically detected galaxies to generate the PDF of q for each target.

For each individual object in our target sample, we select N galaxies from Hsu et al. (2019) that 1) have a specz, and 2) have a photz within 0.5 of the target object's photz. We then define the PDF F(q) to be a sum of Gaussians, where each Gaussian is centered on q_i , which is the value of q for the ith galaxy among the N galaxy subsample of Hsu et al. (2019):

$$F(q) = \frac{1}{\sqrt{2\pi\sigma^2}} \frac{1}{N} \sum_{i=1}^{N} \exp\left[-\frac{(q-q_i)^2}{2\sigma^2}\right].$$
 (A3)

In Equation A3, the Gaussian width σ is the normalized median absolute deviation (NMAD) of the values of q_i among the sample of N galaxies, defined as

$$\sigma \equiv 1.48 \times \text{median} |q_i|_{i=1}^N . \tag{A4}$$

With our PDF defined, the probability of a given galaxy falling within $z_{\min} \leq z \leq z_{\max}$ is then

$$P(z_{\min} \le z \le z_{\max}) = \int_{q_{\min}}^{q_{\max}} F(q) T(q, z_{\text{phot}}) dq, \qquad (A5)$$

where the values of q_{\min} and q_{\max} are calculated from z_{\min} and z_{\max} from Equation A1. $T(q, z_{\text{phot}})$ is a function of redshift that describes whether a galaxy would be detectable with MOSFIRE, based on the observability of strong lines (i.e., [OIII] $\lambda 5008$ and H $\alpha \lambda 6563$) in the K-band. This factor is included so that N_{\exp} is the number of galaxies that we expect to be detected based on their photzs, such that we can accurately calculate $\delta_{\text{gal,obs}}$ using our raw number counts of galaxies in each volume. For simplicity, we assume that T(z) is proportional to the spectroscopic throughput of the telescope, instrument, and atmosphere at the observed wavelengths of these lines for any given redshift. From there, it is straightforward to convert T(z) into $T(q, z_{\text{phot}})$ using Equation A1.

We take N_{exp} to be the sum of these P(z) for all galaxies we observed within a given sky area:

$$N_{\rm exp} = \sum_{j} f_j P_j(z) \,, \tag{A6}$$

where f_j is the MOSFIRE detection fraction for galaxies in our survey with $z_{\text{phot},j} - 0.5 \le z_{\text{phot}} \le z_{\text{phot},j} + 0.5$.

B. MONTE CARLO PROCEDURE

To measure the uncertainties of the measurements produced by this procedure, we run MC simulations varying the values of N_{obs} and N_{exp} as follows:

We assume that $N_{\rm obs}$ follows Poisson statistics (e.g., Gehrels 1986). For each of the MC runs, we draw a value from the Poisson distribution assuming a mean of 13 for GNCL-z3.14, 11 for GNCL-3.10, and 25 for the combined group. These are the number of objects within the volumes outlined in Figure 5 that also have photozs from Hsu et al. (2019). To also vary $N_{\rm exp}$, we draw a random redshift from the PDF given in Equation A5 for each observed galaxy within the 4.3'-radius sky area. Instead of integrating the redshift PDFs for each galaxy, for the MC runs, we count each galaxy whose drawn redshift z_j falls within the redshift range of the protocluster candidate, i.e.,

$$N_{\text{exp}} = \sum_{z_{\text{min}} < z_j < z_{\text{max}}} f_j. \tag{B7}$$

We use this method rather than simply obtaining the posterior P(z) distribution from eazy, as those distributions have a strong dependence on the choice of galaxy templates and the choice of priors used in their fits. Because we base our P(z) function exclusively on the actual differences between $z_{\rm spec}$ and $z_{\rm phot}$ for galaxies fit identically to our targets, and P(z) for an individual object is calculated based on the δz of several hundred objects, this probability is agnostic to these biases.

REFERENCES

- Alberts, S. & Noble, A., 2022, Universe, 8, 554
- Astropy Collaboration, Robitaille, T. P., Tollerud, E. J., et al. 2013, A&A, 558, A33
- Astropy Collaboration, Price-Whelan, A. M., Sipőcz, B. M., et al. 2018, AJ, 156, 123
- Astropy Collaboration, Price-Whelan, A. M., Lim, P. L., et al. 2022, ApJ, 935, 167
- Bahcall, N. A. & Soneira, R. M. 1983, ApJ, 270, 20
- Bahcall, N. A., Dong, F., Hao, L., et al. 2003, ApJ, 599, 814
- Balogh, M. L., Schade, D., Morris, S. L., et al. 1998, ApJ, 504, 75 Balogh, M. L., van der Burg, R. F. J., Muzzin, A., et al. 2021,
- MNRAS, 500, 358
 Parger A. L. Carrie, L. L. & Wang, W. H. 2008, Ap. L. 680
- Barger, A. J., Cowie, L. L., & Wang, W.-H. 2008, ApJ, 689, 687
- Barger, A. J., Cowie, L. L., Chen, C.-C., et al. 2014, ApJ, 784, 9
- Barger, A. J., Cowie, L. L., Blair, A. H., et al. 2022, ApJ, 934, 56
- Barger, A. J. & Cowie, L. L. 2023, 956, 95
- Blain, A. W., Chapman, S. C., Smail, I., et al. 2004, ApJ, 611, 725
- Bleem, L. E., Stalder, B., de Haan, T. et al., 2015, ApJS, 216, 27
 Bothwell, M. S., Smail, I., Chapman, S. C., et al. 2013, MNRAS, 429, 3047
- Brammer, G. B., van Dokkum, P. G., & Coppi, P. 2008, ApJ, 686, 1503
- Brammer, G. B., van Dokkum, P. G., Franx, M., et al. 2012, ApJS, 200, 13
- Brodwin, M., Stanford, S. A., Gonzalez, A. H., et al. 2013, ApJ, 779, 138
- Calvi, R., Castignani, G., & Dannerbauer, H. 2023, A&A, 678, A15
- Carilli, C. L. & Walter, F. 2013, ARA&A, 51, 105
- Casey, C. M. 2012, MNRAS, 425, 3094
- Casey, C. M., Cooray, A., Capak, P., et al. 2015, ApJL, 808, L33Casey, C. M. 2016, ApJ, 824, 36
- Cha, S., HyeongHan, K., Scofield, Z. P., et al. 2024, ApJ, 961, 186
- Chabrier, G. 2003, PASP, 115, 763
- Chapman S. C., Blain A. W., Smail I., & Ivison R. J., 2005, ApJ, 622, 772
- ApJ, 622, 772 Chapman, S. C., Blain, A., Ibata, R., et al. 2009, ApJ, 691, 560
- Chiang, Y.-K., Overzier, R., & Gebhardt, K. 2013, ApJ, 779, 127 Clowe, D., Gonzalez, A., & Markevitch, M. 2004, ApJ, 604, 596
- Cooper, M. C., Newman, J. A., Weiner, B. J., et al. 2008, MNRAS, 383, 1058
- Cooper, M. C., Aird, J. A., Coil, A. L., et al. 2011, ApJS, 193, 14
- Cowie, L. L., Songaila, A., Hu, E. M., et al. 1996, AJ, 112, 839
- Cowie, L. L., Barger, A. J., Hu, E. M., et al. 2004, AJ, 127, 3137
- Cowie, L. L., Barger, A. J., & Songaila, A. 2016, ApJ, 817, 57
- Cowie, L. L., Barger, A. J., Hsu, L.-Y., et al. 2017, ApJ, 837, 139
- Cowie, L. L., Barger, A. J., Bauer, F. E., et al. 2022, ApJ, 939, 5 Cruddace, R., Voges, W., Böhringer, H. et al., 2002, ApJS, 140,
- Cucciati, O., Lemaux, B. C., Zamorani, G., et al. 2018, A&A, 619, A49
- Elbaz, D., Daddi, E., Le Borgne, D., et al. 2007, A&A, 468, 33 Gehrels, N. 1986, ApJ, 303, 336
- Giavalisco, M., Ferguson, H. C., Koekemoer, A. M., et al. 2004, ApJ, 600, L93

- Grogin, N. A., Kocevski, D. D., Faber, S. M., et al. 2011, ApJS, 197, 35
- Harris, C. R., Millman, K. J., van der Walt, S. J., et al. 2020, Nature. 585, 357
- Helton, J. M., Sun, F., Woodrum, C., et al. 2024, ApJ, 962, 124
 Hill, R., Chapman, S., Scott, D., et al. 2020, MNRAS, 495, 3124
- Hodge, J. A., Carilli, C. L., Walter, F., et al. 2013, ApJ, 776, 22
 Hoffman, G. L., Olson, D. W., & Salpeter, E. E. 1980, ApJ, 242, 861
- Hunter, J. D. 2007, Computing in Science and Engineering, 9, 90Hsu, L.-T., Lin, L., Dickinson, M., et al. 2019, ApJ, 871, 233
- Ivison, R. J., Dunlop, J. S., Smail, I., et al. 2000, ApJ, 542, 27
 Jauzac, M., Eckert, D., Schwinn, J., et al. 2016, MNRAS, 463, 3876
- Jones, L. H., Rosenthal, M. J., Barger, A. J., et al. 2021, ApJ, 916, 46
- Kennicutt, R. C. & Evans, N. J. 2012, ARA&A, 50, 531
- Koekemoer, A. M., Faber, S. M., Ferguson, H. C., et al. 2011, ApJS, 197, 36
- Kriek, M., Shapley, A. E., Reddy, N. A., et al. 2015, ApJS, 218, 15
- Lacaille, K. M., Chapman, S. C., Smail, I., et al. 2019, MNRAS, 488, 1790
- Landsman, W. B. 1995, Astronomical Data Analysis Software and Systems IV, 77, 437
- Lahav, O., Lilje, P. B., Primack, J. R., et al. 1991, MNRAS, 251, 128
- $Long,\,A.\,S.,\,Cooray,\,A.,\,Ma,\,J.,\,et\,al.\,\,2020,\,ApJ,\,898,\,133$
- McConachie, I., Wilson, G., Forrest, B., et al. 2022, ApJ, 926, 37
 McLean, I. S., Steidel, C. C., Epps, H., et al. 2010, Proc. SPIE, 7735, 77351E
- McLean, I. S., Steidel, C. C., Epps, H. W., et al. 2012, Proc. SPIE, 8446, 84460J
- Miller, T. B., Hayward, C. C., Chapman, S. C., et al. 2015, MNRAS, 452, 878
- Miller, T. B., Chapman, S. C., Aravena, M., et al. 2018, Nature, 556, 469
- Mo, H. J. & White, S. D. M. 1996, MNRAS, 282, 347
- Morrison, G. E., Owen, F. N., Dickinson, M., et al. 2010, ApJS, 188, 178
- Mortlock, A., McLure, R. J., Bowler, R. A. A., et al. 2017, MNRAS, 465, 672
- Muldrew, S. I., Hatch, N. A., & Cooke, E. A. 2015, MNRAS, 452, 2528
- Muzzin, A., Wilson, G., Yee, H. K. C. et al., 2009, ApJ, 698, 1934
 Oke, J. B., Cohen, J. G., Carr, M., et al. 1995, PASP, 107, 375
 Owen, F. N. 2018, ApJS, 235, 34
- Overzier, R. A. 2016, ARA&A, 24, 14
- Peebles, P. J. E. 1980, Large-Scale Structure of the Universe by Phillip James Edwin Peebles. Princeton University Press, 1980
 Polletta, M., Soucail, G., Dole, H., et al. 2021, A&A, 654, A121
 Stanford, S. A., Romer, A. K., Sabirli, K. et al., 2006, ApJL, 646, L13
- Steidel, C. C., Adelberger, K. L., Dickinson, M., et al. 1998, ApJ, 492, 428
- Sun, F., Helton, J. M., Egami, E., et al. 2024, ApJ, 961, 69Tamura, Y., Kohno, K., Nakanishi, K., et al. 2009, Nature, 459,61

Totsuji, H. & Kihara, T. 1969, PASJ, 21, 221 van der Burg, R. F. J., Hildebrandt, H., & Erben, T. 2010, A&A, 523, A74

Virtanen, P., Gommers, R., Oliphant, T. E., et al. 2020, Nature Methods, 17, 261

Walter, F., Decarli, R., Carilli, C., et al. 2012, Nature, 486, 233
Wang, G. C. P., Hill, R., Chapman, S. C., et al. 2021, MNRAS, 508, 3754